Experimental Study of L-band and S-band SAR Signal Penetration into Soil and Hard Surface

Guanxin Liu [1], Wei Peng [2], Xiaoli Ding [1*], Jun Zhu [2], Haiqiang Fu [3], Rong Zhao [4], Songbo Wu [1]

[1] Dept. of Land Surveying and Geo-Informatics, and The Research Institute for Land and Space, The Hong Kong Polytechnic University, Hong Kong, China – guanxin.liu@connect.polyu.hk, xl.ding@polyu.edu.hk, song.bo.wu@connect.polyu.hk
[2] Dept. of Surveying and Mapping Science and Technology, Changsha University of Science and Technology, Changsha, China – pengwei@csust.edu.cn, jzhu@csust.edu.cn
[3] Dept. of Surveying and Mapping Science and Technology, Central South University, Changsha, China – haiqiangfu@csu.edu.cn
[4] Dept. of Surveying and Mapping Engineering, Central South University of Forestry and Technology, Changsha, China – zhaorong1018@126.com

Keywords: SAR, Signal penetration, Ground-based SAR, Microwave chamber, Subsurface features.

Abstract

The penetration depth of Synthetic Aperture Radar (SAR) signals is a critical parameter for assessing subsurface characteristics and detecting concealed structures. Although numerous empirical and scattering models have been proposed to estimate signal penetration depth (SPD), there remains a lack of understanding of SPD in various settings. In this study, we deployed a ground-based SAR system equipped with L-band (1.5 GHz) and S-band (3.0 GHz) SAR sensors and a microwave anechoic chamber to carry out experimental studies of SPD in soil with different volumetric water content (VWCs) and in hard surfaces of varying thicknesses of gravel and asphalt. At an incidence angle of 40°, the laboratory measurements indicate that the L-band SPDs in homogeneous clay with VWC levels of 4% and 18% are approximately 45–50 cm and 30–35 cm. The L-band signal can penetrate asphalt up to 9 cm, gravel up to 5 cm, and a composited layer of 2 cm gravel and 7 cm asphalt. The S-band can penetrate loose and compacted clay of 20–25 cm and 15–20 cm, respectively. The SPD in silt loam was about 15–20 cm.

1. Introduction

Synthetic Aperture Radar (SAR) signals have some ability of penetration, enabling the investigation of subsurface characteristics. This property makes SAR valuable for various applications. For instance, its strong penetrability is used in forests to estimate underlying topography and forest height (Fu et al., 2018; Peng et al., 2021; Schuler et al., 1996), in deserts to detect paleochannels and assess sand layer thickness (Guo et al., 2000; McCauley et al., 1982; Xiong et al., 2017), in snow-covered regions to infer snow water equivalent and support multi-layer modelling (Shi and Dozier, 2000a, 2000b; Tsai et al., 2019), and in glaciers to determine ice sheet thickness and detect structures beneath the ice (Akbari et al., 2013; Shi and Dozier, 1993; Tebaldini et al., 2016). Therefore, understanding radar signal penetration is crucial for effectively applying SAR techniques across diverse fields.

A wide range of studies have investigated SAR signal penetration depth (SPD) under various conditions, which can be broadly categorized into two types. The first involves obtaining the complex dielectric permittivity of a medium and converting it into SPD using well-established equations (Singh et al., 2022, 2019; Wilheit, 1978). This method is simple and efficient but highly dependent on the accuracy of the permittivity measurement. Common techniques for acquiring soil dielectric permittivity include direct measurement using instruments such as time-domain reflectometry (TDR) and frequency-domain reflectometry (FDR) or estimating soil moisture content and converting it into permittivity through empirical correlations (Topp et al., 1980; Hallikainen et al., 1985; Dobson et al., 1984). Due to the strong sensitivity of backscattering coefficients to soil properties, empirical and semi-empirical models have been developed to establish numerical correlations between backscattering coefficients and soil permittivity (Baghdadi et al., 2016; Oh, 2004; Oh et al., 2009). Additionally, polarimetric decomposition techniques have gained interest in estimating dielectric permittivity in volume-like media (Anconitano et al., 2023; Hajnsek et al., 2003; Shi et al., 2019). The other approach relies on interferometric SAR (InSAR) coherence and phase information to estimate SPD. For example, an infinite volume model has been developed to directly relate SPD to InSAR coherence (Dall, 2007; Liu et al., 2020; Zhu et al., 2023), while InSAR phase, after careful error correction, can also be converted into SPD (Xiong et al., 2017). Despite their usefulness in estimating SPD, these methods have limitations. Model-based methods, such as decomposition and coherence models, as well as phase-based methods, are often affected by model accuracy and external factors, leading to reduced precision. Empirical models, while effective for specific soil types, may perform poorly in other media. Moreover, the aforementioned methods are primarily designed to estimate SPD in loose, volume-like media such as soil, forests, and snow. However, they become less effective when applied to compacted materials or hard surfaces.

This study involved a series of laboratory experiments to quantitatively investigate signal penetration depth in different types of media. We designed a ground-based SAR system equipped with L-band (1.5 GHz) and S-band (3.0 GHz) sensors. When combined with a microwave anechoic chamber, this system enables precise SPD measurement by minimizing background noise and eliminating electromagnetic interference. Dihedral corner reflectors were buried at various depths within the media, and signal penetration was assessed based on SAR amplitude characteristics. We prepared soil samples with different moisture levels, surface roughness, and compositions. For hard surfaces, we used different thicknesses of condensed asphalt, gravel, and composite layers of asphalt and gravel. We hope that these laboratory SPD results will be valuable for

https://doi.org/10.5194/isprs-archives-XLVIII-G-2025-967-2025

research on subsurface structure and property detection, as well as moisture content inversion in natural soils and urban environments.

2. Experimental scheme

2.1 Ground-based SAR system

The ground-based SAR system consisted of two main components: the SAR imaging system and the microwave anechoic chamber, as shown in Fig. 1(a). The imaging system includes a sliding track measuring 5 m in length and 1 m in width, along with a lifting frame system that allows flexible height adjustment. The side and front views of the lifting system are shown in Fig. 1(b) and Fig. 1(c), while the sliding track is depicted in Fig. 1(e). The lifting frame has a minimum height of 1.2 m and a maximum height of 3.2 m (Table 1). The SAR sensor is positioned on the white square area, and the two matched antennas are placed on the rectangular areas in Fig. 1(c). The antennas are spaced 1 m apart to minimize interference. The sliding track speed can be controlled within a range of 0–0.5 m/s, with a control accuracy of 0.1 m/s (Table 2). Both the lifting frame and the sliding track are computer-controlled to ensure repeatable and high-precision measurements. As the SAR sensor moves along the track at a specified speed, a series of radar scans of the sample materials are performed, with each scan processed to generate a single-look complex (SLC) SAR image. In our experiments, we used frequency-modulated continuous wave (FMCW) SAR sensors, including L-band and S-band sensors. Compared to pulse-based SAR systems, FMCW SAR is more suitable for close-range imaging and precise target detection (Ting et al., 2018). The central frequencies of the L-band and S-band SAR sensors were 1.5 GHz and 3 GHz, respectively, with a bandwidth of 400 MHz (Table 3). A 3.5 m (length) × 3.1 m (width) × 3.5 m (height) microwave anechoic chamber is shown in Fig. 1(d). To prevent strong backscattering from the ground surface, we laid a 20 cm layer of natural clay on the bottom.

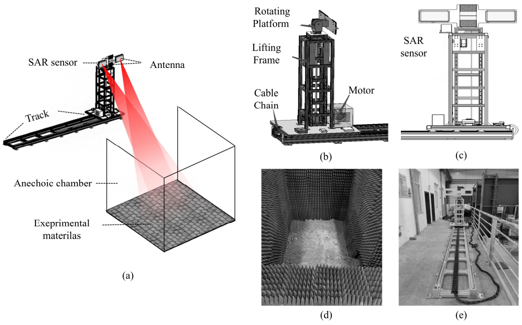

Fig. 1. (a) Experimental setup. (b) and (c) sideview and front view of the ground-based SAR system. (d) the anechoic chamber where soil is at the bottom. (e) sliding track for the radar system.

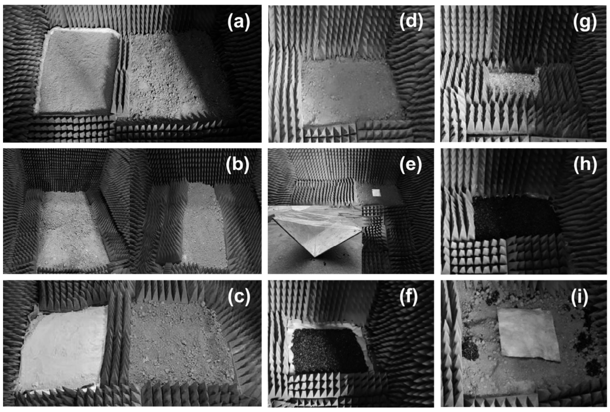

Fig. 2. Photos of experimental sites. (a) clay with 4% (left) and 18% (right) volumetric water content (VWC); (b) 4% VWC clay with different compaction; (c) 4% VWC sandy loam (left) and clay (right); (d) clay at the bottom; (e) a corner reflector to be buried in the materials; (f) asphalt; (g) gravel; (h) a composite layer of asphalt and gravel; (i) fabric covering soils.

Table 1. Specifications of the lifting frame

Item	Metrics	Description
1	Lifting distance	1.2 m
2	Height	2 – 3.2 m
3	Height control accuracy	≤ 0.1 mm
4	Pitch angle	-30° – 90°
5	Pitch control accuracy	0.5°

Table 2. Specifications of the sliding track

Item	Metrics	Description
1	Distance	5 m
2	Speed	0 – 0.5m/s
3	Speed control accuracy	≤ 0.1m/s
4	Positioning accuracy	≤ 5mm
5	Movement smoothness	≤ 5mm
6	Straightness	≤ 10mm
7	Power supply	220V AC
8	Width	1 m

Table 3. Specifications of L-band and S-band SAR sensors

Item	Metrics	S–band	L–band
1	Polarizations	Quad	Quad
2	Nadir angle	Conditional	Conditional
3	Antenna gain	14 dB	10 dB
4	Azimuth beamwidth	15°	30°
5	Range beamwidth	30°	60°
6	Transmit power	5 w	5 w
7	Central frequency	3.0 ± 0.2 GHz	1.5 GHz
8	Bandwidth	400 MHZ	400 MHZ

2.2 Sample materials

Various experimental materials were prepared, including soil and hard surface materials, as shown in Fig. 2. Fig. 2(a) presents two types of natural clay with average VWC of 4% and 18%, respectively. These two VWC levels represent typical soil moisture levels in real-world conditions (Zheng et al., 2023; Han et al., 2023). Fig. 2(b) shows loose clay with 4% VWC on the left and compacted clay on the right. Differences in soil compaction result in variations in surface roughness. Two soil types, clay and silt loam, are displayed in Fig. 2(c). Hard surface materials, including condensed asphalt, gravel, and a composite layer of asphalt and gravel, are shown in Fig. 2(f)–(h). To investigate signal penetrability in these materials, a dihedral corner reflector was obliquely buried in a 10 cm-thick soil layer, as illustrated in Fig. 2(d) and Fig. 2(e). Additionally, to facilitate material handling and adjust material thickness, a fabric layer was placed beneath the hard surface materials, as shown in Fig. 2(i).

2.3 Penetration depth determination

In our experiments, the wavelengths of the L-band and S-band signals were 20 cm and 10 cm, respectively. Both sensors operated at an incidence angle of 40°. Since these system parameters are fixed for a given SAR sensor, the echo power primarily depends on the properties of the ground objects. Signal penetration depth (SPD) is defined as the distance within a medium at which the echo power of the propagating radiation is reduced by approximately 63% due to attenuation (Nikita Basargin et al., 2024).

$$P_p = P_{op} * \gamma * e^{-2jk_z d_{pen}} \qquad (1)$$

where P_p is the received power of an EM wave of a known polarization p transmitted at a certain depth, P_{op} is the power of the incident wave, γ represents the transmissivity at the air-soil interface and k_z is the wavenumber in medium. d_{pen} is the SPD in vertical direction. When $P_p / (P_{op} * \gamma)$ reaches e^{-1}, the penetration depth of SAR signals can be finally determined. However, in real cases, it’s impossible to determine the propagation distance when the signal power reduces to 37% of the incident power. In our experiments, the SPD was determined by measuring the backscatter strength of the dihedral corner reflector buried at various depths in sample materials. Theoretically, as the reflectors are buried deeper, their backscatter signal strength decreases compared to that of reflectors on the bare surface and the background response of the medium. Finally, when the maximum penetration depth is achieved, the burial reaches a level where the backscatter signal strength equals or closes to the background soil signal (Muskett, 2017). To minimize potential errors, the region of interest was scanned twice during each test.

3. Results

3.1 L-band penetration

Before carrying out experiments, two corner reflectors were positioned at opposite diagonal corners within the chamber area to establish effective boundaries. Subsequent analysis was focused on this delineated region. Prior to conducting tests on soil and hard surface penetration, a preliminary examination of the backscattering characteristics of both the corner reflectors and background materials was undertaken. This step was followed by increasing the thickness of the medium. In each test, a sequence of SAR amplitude images was acquired. The backscattering power was then computed and represented in decibels (dB) to ensure a more uniform distribution of values and mitigate outliers. A comprehensive summary of the penetration results of L-band and S-band SAR signals across various media is provided.

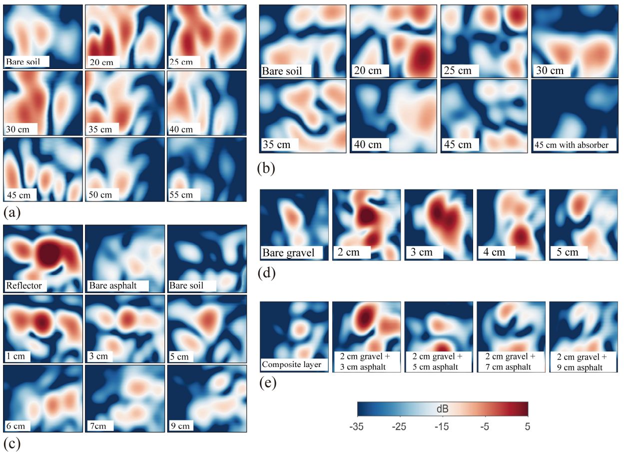

Fig. 3. Amplitudes of L-band scattered signals. (a) 4% VWC clay. (b) 18% VWC clay. (c) asphalt. (d) gravel. (e) the composite layer of varying thickness of asphalt and gravel.

3.1.1 Clays with different moisture contents: The penetration results in 4% and 18% VWC clays are shown in Fig. 3(a) and (b). The backscattering intensity of bare soils is displayed in the first subplot, from which we can observe similar signal responses with majority values ranging from -22 dB to -10 dB. We used this background response as the reference and then added the thickness of clays to observe the backscattering difference. In both tests, the first thickness level was set as 20 cm. The corner reflector was then placed under a thickness of 20 cm-thick soil and the signal response was recorded. The increased thickness gradient is 5 cm each time.

For soil with a 4% VWC, the highest radar backscatter strength was recorded when the dihedral corner reflector was buried at a depth of 20 cm. As the soil thickness increased, the backscatter intensity gradually diminished, eventually stabilizing at approximately 45 cm. When the burial depth exceeded 45 cm, the backscatter strength closely resembled that of the bare soil. To provide a quantitative analysis of the penetration results, violin plots were generated, as illustrated in Fig. 5. These plots effectively visualize the distribution of radar backscatter strength. The leftmost section presents a box plot, the central portion features a scatter density map, and the right section includes a histogram with multiple peaks indicating data concentration. A white circle within the scatter density map represents the mean value of all data points ranging from 80% to 100% of the peak intensity, while a connecting line illustrates the variation trend with increasing burial depth. As the soil thickness increased from 20 cm to 45 cm, the backscatter strength steadily declined until reaching a stable level, as shown in Fig. 5(a). Based on these findings, it can be concluded that once the soil thickness reaches 45 cm, the backscatter signal strength becomes indistinguishable from the surrounding soil background. Consequently, the penetration depth of L-band signals in 4% VWC clay is determined to be 45 cm–50 cm.

In soil with an 18% VWC, radar signal strength declines more sharply than in 4% VWC soil (Fig. 3(a)), particularly within the range of 20 cm to 30 cm. Between 30 cm and 35 cm, the rate of intensity reduction slows, eventually stabilizing over the next 10 cm until it reaches a level comparable to the background response. Variations in spatial patterns are also observable in

Fig. 5(b). Based on these findings, the estimated penetration depth in 18% VWC clay is approximately 30 cm–35 cm. At the end of the L-band penetration experiments, a controlled test was conducted to validate the reliability of the backscatter response using the ground-based SAR system. This was achieved by covering a 45 cm-thick clay layer with an L-band absorber. The results showed a significant reduction in signal strength compared to uncovered soil, confirming that the imaging experiments effectively captured real variations in the test area.

3.1.2 Hard surfaces: Constructing a real road within the chamber for signal penetration was not feasible, therefore, typical road materials were used to simulate real road conditions and simplify the penetration experiment. In this study, asphalt and gravel were selected as substitutes. Initially, penetration tests were conducted separately on asphalt and gravel. Subsequently, composite layers of varying thicknesses, consisting of both materials, were prepared to simulate real road conditions. Although real roads feature more complex compositions and undergo intricate construction processes, this experiment still serves as a reference for understanding the penetrability of SAR signals on hard surfaces. Given its superior penetration capability compared to S-band signals, only long-wavelength L-band signals were utilized. Since the corner reflector was securely positioned within the soil (Fig. 2(e)), the backscattering response of both the reflector and the background materials was investigated, as shown Fig. 3(c). The radar backscatter strength of bare asphalt was slightly higher than that of bare 4% VWC soil, though both were significantly lower than that of the corner reflector.

As the asphalt thickness increased from 1 cm to 9 cm, the radar backscatter intensity declined rapidly, reaching a level comparable to bare asphalt when the thickness reached 9 cm. To ensure consistency with real-world hard surfaces, the asphalt was compacted after each incremental increase in thickness. Based on these results, the penetration depth in condensed asphalt was determined to be 9 cm. In the case of gravel, it is evident that its backscatter intensity exceeds that of asphalt when both materials have the same thickness. This conclusion is supported by both the observed changes in spatial patterns (Fig. 3(d)) and the statistical results in Fig. 5(c) and (d). We deduce that the penetration depth of L-band signals in gravel is approximately 5 cm.

Finally, a composite layer consisting of both asphalt and gravel was constructed, with the gravel layer positioned at the bottom and covered by the asphalt layer (Fig. 2(h)). The thickness of the gravel layer was kept constant at 2 cm, while the asphalt thickness ranged from 2 cm to 9 cm. When the asphalt thickness reached 7 cm, the backscatter response became comparable to that of the bare composite layer and remained consistent as the asphalt thickness increased further. The penetration test indicated that the L-band signal was able to penetrate a composite layer composed of 2 cm of gravel and 7 cm of asphalt. In real-world conditions, this penetration depth would be lower, as the materials used in asphalt and cement roads have been carefully proportioned and subjected to multiple processes, such as mixing and compaction.

3.2 S-band penetration

Soil roughness is another critical parameter influencing signal penetrability, and it was therefore evaluated using S-band SAR signals. For this experiment, 4% VWC soils with different compaction levels were prepared, as depicted in Fig. 2(b). As shown in Fig. 4(a) and (b), the backscatter strength of bare compacted soil was slightly higher than that of loose soil. The thickness of both soils was incrementally increased by 5 cm, with the starting point at 10 cm for compacted soil and 15 cm for loose soil. In the compacted soil, a backscattering response similar to that of bare soil was observed as the soil thickness reached 20 cm, which then stabilized over the subsequent 10 cm thickness. Based on these observations, the SPD in compacted soil was determined to be 15 cm–20 cm. Similarly, in loose soil, the backscatter strength gradually decreased until the soil thickness reached 25 cm. The SPD was finally determined as 20 cm–25 cm. Unfortunately, soil roughness parameters, such as the root mean square height and the correlation length, were not measured, limiting the explicit applicability of the derived penetration depths. Nevertheless, the quantitative results indicate that soil compaction has a notable effect on signal penetration.

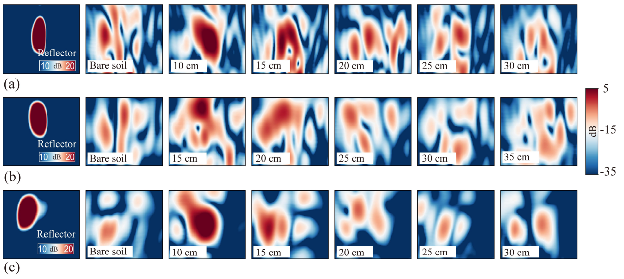

Fig. 4. Amplitudes of S-band scattered signals in materials of 4% VWC. (a) compacted clay. (b) loose clay. (c) silt loam.

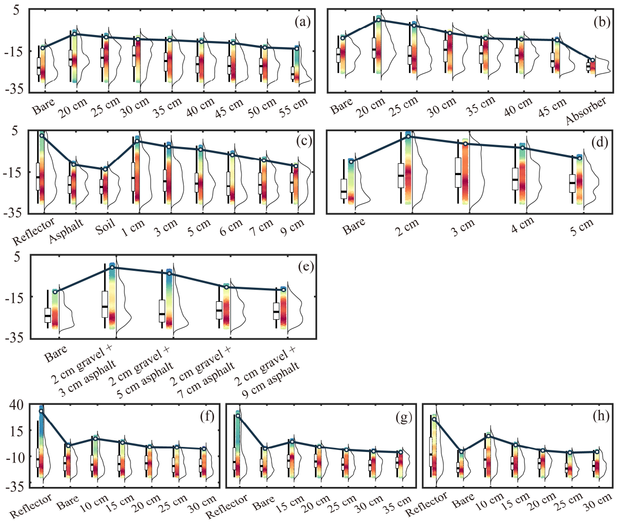

Fig. 5. L-band and S-band signal penetration results into varying media. Each plot is composed of a box plot, a scatter density map and a histogram. The white circle represents the average of all values between 80% and 100% of the maximum intensity.

The same 4% VWC loose soil was used again for comparison, alongside a second soil type, sandy loam, as shown on the left in Fig. 2(c). Sandy loam is a composite material primarily composed of loam with smaller amounts of sand. Its particle size is fine, and the distribution is dense and uniform. The backscatter intensity of bare sandy loam and bare loose soil was comparable, as illustrated in Fig. 4(b) and (c). The signal response in the sandy loam was relatively strong up to a thickness of 15 cm, after which it declined over the next 5 cm. As the thickness increased to 20 cm and 35 cm, the backscatter strength remained nearly constant. The SPD was finally determined as 15 cm–20 cm

4. Conclusions

This experimental study investigates the penetrability of L-band and S-band signals under various conditions using a ground-based SAR system. The study provides quantitative penetration results across different kinds of materials. Laboratory measurements at a constant incidence angle revealed that soil moisture content significantly affects SAR signal penetrability. Additionally, factors such as soil compaction and soil type were also found to play crucial roles in influencing the penetration depth of the signals. The experimental findings further demonstrated that L-band SAR signals are capable of penetrating a certain thickness of hard materials, such as asphalt and gravel. This study offers a more comprehensive understanding of the behaviour of L-band and S-band SAR signals in typical natural scenarios. The quantitative results are intended to provide researchers with valuable insights into detecting the internal properties of subsurface layers. Future research will explore the penetrability of SAR signals at various incidence angles. Additionally, improvements to the ground-based system and experimental conditions will facilitate the investigation of signal penetrability in a wider range of scenarios and materials.

References

Akbari, V., Doulgeris, A.P., Eltoft, T., 2013. Monitoring glacier changes using multitemporal multipolarization SAR images. IEEE Trans. Geosci. Remote Sens. 52, 3729–3741. https://doi.org/10.1109/TGRS.2013.2275203

Anconitano, G., Lavalle, M., Acuña, M.A., Pierdicca, N., 2023. Sensitivity of polarimetric SAR decompositions to soil moisture and vegetation over three agricultural sites across a latitudinal gradient. IEEE J. Sel. Top. Appl. Earth Obs. Remote Sens. 17, 3615–3634. https://doi.org/10.1109/JSTARS.2023.3332423

Baghdadi, N., Choker, M., Zribi, M., Hajj, M.E., Paloscia, S., Verhoest, N.E., Lievens, H., Baup, F., Mattia, F., 2016. A new empirical model for radar scattering from bare soil surfaces. Remote Sens. 8, 920. https://doi.org/10.3390/rs8110920

Basargin, N., Alonso-González, A., Hajnsek, I., 2024. Comparison of interferometric soil moisture model and F-SAR data over agricultural areas at C- and L-bands. In: IGARSS 2024-2024 IEEE Int. Geosci. Remote Sens. Symp. IEEE, pp. 10715–10718. https://doi.org/10.1109/IGARSS53475.2024.10640376

Dall, J., 2007. InSAR elevation bias caused by penetration into uniform volumes. IEEE Trans. Geosci. Remote Sens. 45, 2319–2324. https://doi.org/10.1109/TGRS.2007.896613

Dobson, M.C., Kouyate, F., Ulaby, F.T., 1984. A reexamination of soil textural effects on microwave emission and backscattering. IEEE Trans. Geosci. Remote Sens. 530–536. https://doi.org/10.1109/TGRS.1984.6499165

Fu, H.Q., Zhu, J.J., Wang, C.C., Zhao, R., Xie, Q.H., 2018. Underlying topography estimation over forest areas using single-baseline InSAR data. IEEE Trans. Geosci. Remote Sens. 57, 2876–2888. https://doi.org/10.1109/TGRS.2018.2878357

Guo, H., Liu, H., Wang, X., Shao, Y., Sun, Y., 2000. Subsurface old drainage detection and paleoenvironment analysis using spaceborne radar images in Alxa Plateau. Sci. China Ser. D-Earth Sci. 43, 439–448. https://doi.org/10.1007/BF02959455

Hajnsek, I., Pottier, E., Cloude, S.R., 2003. Inversion of surface parameters from polarimetric SAR. IEEE Trans. Geosci. Remote Sens. 41, 727–744. https://doi.org/10.1109/TGRS.2003.810702

Hallikainen, M.T., Ulaby, F.T., Dobson, M.C., El-Rayes, M.A., Wu, L.-K., 1985. Microwave dielectric behavior of wet soil—Part I: Empirical models and experimental observations. IEEE Trans. Geosci. Remote Sens. 25–34. https://doi.org/10.1109/TGRS.1985.289497

Han, Q., Zeng, Y., Zhang, L., Wang, C., Prikaziuk, E., Niu, Z., Su, B., 2023. Global long-term daily 1 km surface soil moisture dataset with physics-informed machine learning. Sci. Data 10, 101. https://doi.org/10.1038/s41597-023-02011-7

Liu, G., Fu, H., Zhu, J., Wang, C., Xie, Q., 2020. Penetration depth inversion in hyperarid desert from L-band InSAR data based on a coherence scattering model. IEEE Geosci. Remote Sens. Lett. 18, 1981–1985. https://doi.org/10.1109/LGRS.2020.3011706

McCauley, J.F., Schaber, G.G., Breed, C.S., Grolier, M.J., Haynes, C.V., Issawi, B., Elachi, C., Blom, R., 1982. Subsurface valleys and geoarcheology of the eastern Sahara revealed by shuttle radar. Science 218, 1004–1020. https://doi.org/10.1126/science.218.4576.1004

Muskett, R.R., 2017. L-Band InSAR Penetration Depth Experiment, North Slope Alaska. J. Geosci. Environ. Prot. 5, 14. https://doi.org/10.4236/gep.2017.53002

Oh, Y., 2004. Quantitative retrieval of soil moisture content and surface roughness from multipolarized radar observations of bare soil surfaces. IEEE Trans. Geosci. Remote Sens. 42, 596–601. https://doi.org/10.1109/TGRS.2003.821065

Oh, Y., Hong, S.-Y., Kim, Y., Hong, J.-Y., Kim, Y.-H., 2009. Polarimetric backscattering coefficients of flooded rice fields at L- and C-bands: Measurements, modeling, and data analysis. IEEE Trans. Geosci. Remote Sens. 47, 2714–2721. https://doi.org/10.1109/TGRS.2009.2014053

Peng, X., Long, S., Wang, Y., Xie, Q., Du, Y., Pan, X., 2021. Underlying topography inversion using dual polarimetric TomoSAR. Sensors 21, 4117. https://doi.org/10.3390/s21124117

Schuler, D.L., Lee, J.-S., De Grandi, G., 1996. Measurement of topography using polarimetric SAR images. IEEE Trans. Geosci. Remote Sens. 34, 1266–1277. https://doi.org/10.1109/36.536542

Shi, H., Yang, J., Li, P., Zhao, L., Liu, Z., Zhao, J., Liu, W., 2019. Soil moisture estimation using two-component decomposition and a hybrid X-Bragg/Fresnel scattering model. J. Hydrol. 574, 646–659. https://doi.org/10.1016/j.jhydrol.2019.04.049

Shi, J., Dozier, J., 1993. Measurements of snow- and glacier-covered areas with single-polarization SAR. Ann. Glaciol. 17, 72–76. https://doi.org/10.3189/S0260305500012635

Shi, J., Dozier, J., 2000a. Estimation of snow water equivalence using SIR-C/X-SAR. I. Inferring snow density and subsurface properties. IEEE Trans. Geosci. Remote Sens. 38, 2465–2474. https://doi.org/10.1109/36.885195

Shi, J., Dozier, J., 2000b. Estimation of snow water equivalence using SIR-C/X-SAR. II. Inferring snow depth and particle size. IEEE Trans. Geosci. Remote Sens. 38, 2475–2488. https://doi.org/10.1109/36.885196

Singh, A., Meena, G.K., Kumar, S., Gaurav, K., 2019. Evaluation of the penetration depth of L- and S-band (NISAR mission) microwave SAR signals into ground. In: 2019 URSI Asia-Pacific Radio Science Conference (AP-RASC). IEEE, pp. 1–1.

Singh, A., Niranjannaik, M., Kumar, S., Gaurav, K., 2022. Comparison of different dielectric models to estimate penetration depth of L- and S-band SAR signals into the ground surface. Geographies 2, 734–742. https://doi.org/10.3390/geographies2040045

Tebaldini, S., Nagler, T., Rott, H., Heilig, A., 2016. Imaging the internal structure of an alpine glacier via L-band airborne SAR tomography. IEEE Trans. Geosci. Remote Sens. 54, 7197–7209. https://doi.org/10.1109/TGRS.2016.2597361

Ting, J.-W., Oloumi, D., Rambabu, K., 2018. FMCW SAR system for near-distance imaging applications—practical considerations and calibrations. IEEE Trans. Microw. Theory Tech. 66, 450–461. https://doi.org/10.1109/TMTT.2017.2706693

Topp, G.C., Davis, J.L., Annan, A.P., 1980. Electromagnetic determination of soil water content: Measurements in coaxial transmission lines. Water Resour. Res. 16, 574–582. https://doi.org/10.1029/WR016i003p00574

Tsai, Y.-L.S., Dietz, A., Oppelt, N., Kuenzer, C., 2019. Remote sensing of snow cover using spaceborne SAR: A review. Remote Sens. 11, 1456. https://doi.org/10.3390/rs11121456

Wilheit, T.T., 1978. Radiative transfer in a plane stratified dielectric. IEEE Trans. Geosci. Electron. 16, 138–143. https://doi.org/10.1109/TGE.1978.294577

Xiong, S., Muller, J.-P., Li, G., 2017. The application of ALOS/PALSAR InSAR to measure subsurface penetration depths in deserts. Remote Sens. 9, 638. https://doi.org/10.3390/rs9060638

Zheng, C., Jia, L., Zhao, T., 2023. A 21-year dataset (2000–2020) of gap-free global daily surface soil moisture at 1-km grid resolution. Sci. Data 10, 139. https://doi.org/10.1038/s41597-023-01991-w

Zhu, J., Liu, G., Zhao, R., Ding, X., Fu, H., 2023. ML-based approach for inverting penetration depth of SAR signals over large desert areas. Remote Sens. Environ. 295, 113643. https://doi.org/10.1016/j.rse.2023.113643